Published in final edited form as:

Nature. 2019 May ; 569(7755): 289–292. doi:10.1038/s41586-019-1144-0.

XFEL structures of the human MT_2 melatonin receptor reveal basis of subtype selectivity

Linda C. Johansson[1,†], **Benjamin Stauch**[1,†], **John D. McCorvy**[2,11], **Gye Won Han**[1], **Nilkanth Patel**[1], **Xi-Ping Huang**[2,3], **Alexander Batyuk**[4], **Cornelius Gati**[5,6], **Samuel T. Slocum**[2], **Chufeng Li**[7,8], **Jessica M. Grandner**[1], **Shuming Hao**[1], **Reid H.J. Olsen**[2], **Alexandra R. Tribo**[2], **Sahba Zaare**[7], **Lan Zhu**[8], **Nadia A. Zatsepin**[7,8], **Uwe Weierstall**[7,8], **Saïd Yous**[9], **Raymond C. Stevens**[1], **Wei Liu**[7], **Bryan L. Roth**[2,3,10,*], **Vsevolod Katritch**[1,*], and **Vadim Cherezov**[1,*]

[1]Bridge Institute, Departments of Chemistry and Biological Sciences, University of Southern California, Los Angeles, CA, USA

[2]Department of Pharmacology, University of North Carolina at Chapel Hill, Chapel Hill, NC, USA

[3]National Institute of Mental Health Psychoactive Drug Screening Program (NIMH PDSP), University of North Carolina at Chapel Hill, Chapel Hill, NC, USA

[4]Linac Coherent Light Source, SLAC National Accelerator Laboratory, Menlo Park, CA, USA

[5]SLAC National Accelerator Laboratory, Bioscience Division, Menlo Park, CA, USA

[6]Stanford University, Department of Structural Biology, Stanford, CA, USA

[7]Department of Physics, Arizona State University, Tempe, AZ, USA

[8]School of Molecular Sciences and Biodesign Center for Applied Structural Discovery, Biodesign Institute, Arizona State University, Tempe, AZ, USA

[9]Université de Lille, CHU Lille, Inserm, UMR-S 1172 - JPArc - Centre de Recherche Jean-Pierre AUBERT Neurosciences et Cancer, Lille, France

[*]Correspondence to V.C. (cherezov@usc.edu), B.L.R. (bryan_roth@med.unc.edu), and V.K. (katritch@usc.edu).
[†]These authors contributed equally to this work.

Author contributions L.C.J., B.S., V.K., and V.C. conceived the project, analysed data, and wrote the paper with contributions from all authors. L.C.J. and B.S. designed, optimised, purified and characterised receptor constructs for structural studies and crystallised the receptor, prepared crystal samples and figures, solved and refined the structures, and assisted in generating mutant constructs for binding and functional analyses. J.D.M., X.P.H., and S.T.S. performed radioligand binding and functional experiments, assisted in making mutant and wild-type constructs, and analysed binding and functional data. L.C.J., B.S., A.B., L.Z., W.L., and V.C. collected XFEL data. S.Z. and U.W. operated the LCP injector during XFEL data collection. S.H., L.Z., and W.L. assisted in XFEL sample preparation. A.B., C.G, C.L., and N.A.Z. processed XFEL data. L.C.J., G.W.H. and A.B. determined the structures. L.C.J. and G.W.H. performed the structure refinement and quality control. N.P., J.M.G., and V.K. designed mutants for radioligand and functional studies, performed molecular docking and molecular dynamics simulations. R.H.J.O. and A.R.T. assisted with molecular biology and functional experiments. S.Y. synthesised the bitopic compound, analysed data, and edited the paper. R.C.S. supervised protein expression and edited the paper. B.L.R. supervised pharmacological experiments and edited the paper. V.K. supervised molecular docking and molecular dynamics calculations. V.C. coordinated and supervised the whole project.

Data availability Structure factors and coordinates were deposited in the Protein Data Bank under the following accession codes: 6ME6 (MT_2-CC-2-pmt), 6ME7 (MT_2-CC-H208A-2-pmt), 6ME8 (MT_2-CC-N86D-2-pmt), 6ME9 (MT_2-CC-ramelteon).

The authors declare no competing interests.

[10]Division of Chemical Biology and Medicinal Chemistry, Eshelman School of Pharmacy, University of North Carolina at Chapel Hill, Chapel Hill, NC, USA

[11]Current address: Department of Cell Biology, Neurobiology and Anatomy, Medical College of Wisconsin, Milwaukee, WI, USA

Abstract

The human MT_1[1] and MT_2[2] melatonin receptors are G protein-coupled receptors (GPCRs) involved in the regulation of circadian rhythm and sleep patterns[3]. Drug development efforts target both receptors for treatment of insomnia, circadian rhythm and mood disorders, and cancer[3], while MT_2 has also been implicated in type 2 diabetes (T2D)[4,5]. Here we report the X-ray Free Electron Laser (XFEL) structures of the human MT_2 receptor in complex with agonists 2-phenylmelatonin (2-pmt) and ramelteon[6] at resolutions of 2.8 Å and 3.3 Å, respectively, along with two structures of function-related mutants, $H208^{5.46}A$ (superscripts represent the Ballesteros-Weinstein residue numbering nomenclature[7]) and $N86^{2.50}D$, obtained in complex with 2-pmt. Comparison of the MT_2 structures with MT_1[8] reveals that, despite the fact that the orthosteric ligand-binding site residues are conserved, there are notable conformational variations as well as differences in [^{3}H]-melatonin dissociation kinetics that provide new insights into the selectivity between melatonin receptor subtypes. In addition to the membrane-buried lateral ligand entry channel that is also observed in MT_1, the MT_2 structures reveal a narrow opening towards the solvent in the extracellular part of the receptor. We provide functional and kinetic data supporting a prominent role for the intramembrane ligand entry in both receptors, while simultaneously suggesting the possibility of an extracellular entry path in MT_2. Our findings contribute to a molecular understanding of melatonin receptor subtype selectivity and ligand access modes, which are essential for the design of highly selective melatonin tool compounds and therapeutic agents.

To enhance low surface expression and stability of the wild-type receptor, eight point mutations were introduced based on homology to other class A receptors: $D86^{2.50}N$[9], $L108^{ECL1}F$, $F129^{3.41}W$[10], $N137^{3.49}D$, $C140^{3.52}L$, $W264^{6.48}F$, $A305^{7.50}P$, and $N312^{8.47}D$, which were essential for high-resolution structure determination of MT_2 as well as MT_1[8]. To promote crystal contacts, we used a double-fusion approach, with rubredoxin[11] in the intracellular loop 3 (ICL3) and thermostabilised apocytochrome b_{562}RIL (BRIL)[11], attached to the receptor N-terminus. Radioligand binding assays revealed a 120-fold reduction of melatonin binding affinity (~30-fold reduction at physiological concentration of NaCl), likely due to the stabilisation of the crystallised construct in an inactive “low agonist affinity” state deficient of G-protein coupling and signaling[9,12] (Extended Data Table 1). All four MT_2 structures were obtained using lipidic cubic phase (LCP)[13] crystallisation (Extended Data Fig. 1, Extended Data Table 2). The overall receptor conformation was found to be similar in all four structures (Cα r.m.s.d. < 0.3 Å), therefore the highest resolution MT_2-2-pmt structure is used in the analysis below unless otherwise noted.

MT_2 adopts the canonical 7TM-fold of class A receptors, with the short amphipathic helix VIII parallel to the membrane on the intracellular side (Fig. 1a). Like in MT_1[8], the 7TM bundle of MT_2 is found in inactive conformation. Restoring the function-impairing $D86^{2.50}N$ mutation (Extended Data Table 3) allowed us to solve the MT_2-N86D-2-pmt

structure at lower resolution, revealing no significant effect of this mutation on the overall receptor conformation, as also supported by molecular dynamics (MD) simulations (Supplementary Fig. 1). Structural comparison of MT_2 vs. MT_1, which share 68% sequence identity, reveals a remarkable overall similarity (Cα r.m.s.d. < 0.6 Å), with all ligand-interacting residues conserved[8] (Fig. 1d, Extended Data Fig. 2c). We observe a common pharmacophore between receptor subtypes that consists of aromatic stacking of the ligand core with $F192^{ECL2}$, as well as hydrogen bonds between the methoxy group of 2-pmt and $N175^{4.60}$ and between the ligand alkylamide tail and $Q194^{ECL2}$ (Fig. 1c, d). Stability of these ligand-anchoring interactions is confirmed by MD simulations (Extended Data Fig. 3). Further, mutating $F192^{ECL2}$ to isoleucine or alanine causes loss of ligand binding and signaling (Extended Data Tables 1, 4), as also observed for MT_1[8]. In contrast to MT_1, however, mutating $N175^{4.60}$ to alanine retains receptor function, pointing to a different role of this residue in the activation of the two receptor subtypes. While mutating either $Q194^{ECL2}$ or $N268^{6.52}$ to alanine only has minor effects on receptor ligand affinity, receptor activation, or stability (Extended Data Tables 1, 4, 5), the double mutant $Q194^{ECL2}$A/$N268^{6.52}$A results in a dramatic loss of receptor activity (Extended Data Tables 4, 5), suggesting a functional redundancy of these residues in MT_2. Intriguingly, despite the binding site residues being conserved between the two receptors, we observe subtle conformational differences, such as in the side chains of $Y200^{5.38}$, $Y294^{7.39}$ and the backbone region surrounding $P174^{4.59}$ (Extended Data Fig. 2d). Furthermore, the MT_2 binding pocket is about 50 $Å^3$ (7 %) larger than that of MT_1, with most of the volume difference attributed to the region around the alkylamide tail and the hydrophobic sub-pocket that accommodates substituents of melatonin analogues in our structures (Fig. 1d, Extended Data Fig. 2b) and plays a key role in MT_2 selectivity as further discussed.

Structural analysis of MT_2 reveals an opening between helices IV and V from the orthosteric ligand binding site to the membrane (Fig. 2a). This channel is similar to the one observed in MT_1, but more constricted (~2.6 Å in diameter at the narrowest part). A comparison between the MT_2 and MT_1 structures reveals that $Y200^{5.38}$ in MT_2 makes a hydrogen bond to $N175^{4.60}$, constricting the channel, while in MT_1 it adopts a different conformation pointing towards the lipid interface (Fig 2a–c, Extended Data Fig. 2c, d). Close to the entrance is $H208^{5.46}$, which in our MT_2-H208A-2-pmt structure further closes off the opening by an ~0.9 Å inward shift of helix V (Extended Data Fig. 4), suggesting that this residue plays a role in controlling the channel entrance, albeit only moderately influencing ligand affinity and receptor function in MT_2 (Extended Data Table 1, 4). Further analysis of the MT_2 structures reveals a potential secondary access route to the orthosteric binding site from the solvent-exposed extracellular (ECL) region (Fig. 2d). This second opening has a slightly larger diameter (~2.5–3 Å) and is lined by aromatic $Y294^{7.39}$ and hydrophilic $T191^{ELC2}$, $Q194^{ECL2}$ residues (Fig. 2e). In MT_1, the corresponding residues $Q181^{ECL2}$ and $Y281^{7.39}$ adopt different conformations, completely sealing off this entrance (Fig. 2f).

To test the relative importance of these two putative binding site access routes we performed kinetic ligand dissociation studies on both receptors using [^{3}H]-melatonin as a tracer. The ligand residence time (k_{off}^{-1}) in wild-type MT_2 is substantially longer than that in MT_1, suggesting that the narrower membrane entry channel indeed restricts ligand access (Fig. 2g, h). Mutation of the membrane channel-lining residue $Y^{5.38}$A, designed to widen the access

channel, shows a drastic 30-fold decrease in residence time for MT_2 (with a similar ligand affinity), while the corresponding mutation in MT_1 displays a more modest decrease in residence time, in agreement with the wider channel and a different conformation of $Y^{5.38}$ in MT_1. To constrict the channel, we mutated $A^{4.56}$, a critical residue at the interface of helices IV and V in both receptors, into a bulkier methionine. Strikingly, this mutation dramatically increases residence time for both receptors (Fig. 2g, h), reaching up to 20 hours in MT_2, suggesting a prominent role of this channel for ligand access in both receptors.

For mutants designed to widen the ECL opening in both receptors, ligand residence time was reduced more than 10-fold at MT_2 mutants $T191^{ECL2}A$ and $Q194^{ECL2}A$, and roughly 5-fold at equivalent ECL2 mutants in MT_1 (Fig. 2g, h). Mutating $Y294^{7.39}A$ in MT_2 showed even greater decrease in ligand residence time (22-fold) relative to wild-type, while the equivalent mutant in MT_1 showed similar residence time to wild-type. These differences can be reconciled by a higher importance of the ECL ligand site access in MT_2 compared to MT_1 in agreement with the crystal structures, where residue $Y294^{7.39}$ adopts a different conformation in MT_2, allowing for easier ligand egress through the ECL opening.

The elucidation of high-resolution structures of both melatonin receptor subtypes and published ligand structure-activity relationship (SAR) data[14,15] allowed us to establish a model of receptor subtype ligand selectivity. To this end, we utilised molecular docking of several available selective ligands to both receptors. Docking of the moderately MT_1-selective compound 5-HEAT[16] and bitopic ligand CTL 01–05-B-A05[8] suggests that although an extension or substitution of the R^1 position by a linear alkyl chain can be accommodated by the membrane access channel in both MT_1 and MT_2 (Fig. 3a, c), the narrower MT_2 channel renders binding of the extended portion of the bitopic ligands suboptimal due to potential steric clashes. Accordingly, an $H208^{5.46}A$ mutation in MT_2 abolished G_i-agonist efficacy of the bitopic ligand CTL 01–05-B-A05 (Extended Data Fig. 4d), likely by further restricting the channel and/or eliminating the hydrogen bond between $H208^{5.46}$ and CTL 01–05-B-A05, observed in docking to MT_1[8]. This mutation had negligible effect on monotopic ligand binding and function (Extended Data Tables 1, 4, 5), suggesting that a sufficiently wide membrane channel (as in MT_1) is critical for accommodation of bitopic ligands.

The MT_2-selective ligands IIK7 and DH97 (both ~90-fold selective)[17,18] adopt “tail up” binding modes similar to that of 2-pmt with their alkylamide tails (R^2 position in Fig. 3b, c) interacting with $Q194^{ECL2}$. In contrast, in MT_1 the longer alkylamide tails of these ligands avoid such upward tail position due to steric clashes and can only adopt suboptimal “tail down” conformations. Bulky substituents in the R^3 position confer MT_2 selectivity by utilising the larger hydrophobic sub-pocket of the receptor (Fig. 3b, c). In summary, our analysis suggests that R^1 substituents are important for MT_1 selectivity, while R^2 and R^3 mostly convey selectivity towards MT_2 (Fig. 3c). The slightly larger binding site in MT_2 also helps to achieve selectivity, as reflected by the larger number of compounds moderately selective for MT_2 (Extended Data Fig. 5).

Subtype-selective compounds are desirable due to the involvement of MT_2 in T2D, where a number of single nucleotide polymorphisms (SNPs) have been reported[4,5]. Mapping these

sites onto our MT_2 structure, we observed clustering of residues in the vicinity of the ligand binding pocket and on the receptor surface, along the membrane interface of helices I and II and the intracellular G protein and β-arrestin binding regions (Fig. 4). The exposed positions of these residues could point to their involvement in interactions with intracellular and membrane partners. Other instances of T2D SNPs include P95$^{2.59}$L of the YPYP motif, which was found to play a role in receptor stability and function in MT_1[8], and mutations in known microswitches such as R138$^{3.50}$H/L/C of the E/DRY motif[19] and Y308$^{7.53}$S of the NPxxY motif[12]. While none of the analysed SNPs is involved in direct interactions with melatonin, the M120I and V124I variants are located in the hydrophobic sub-pocket of the receptor, which could influence ligand binding and affect subsequent signaling pathways[4,5].

The structural basis for melatonin receptor subtype selectivity revealed here has the potential to inspire a new generation of highly selective pharmacological tools that will help to further dissect the melatonin system. We also provide insights into differences in ligand entry between the two receptors by demonstrating the potential of MT_2 to support extracellular ligand access to the binding pocket. This difference in ligand entry can be exploited to facilitate melatonin receptor subtype selectivity, as the ECL route in MT_2 could accommodate more polar compounds compared to the membrane-buried channel. We therefore expect that our results will lead to new therapies involving these pleiotropic receptors, aimed at but not limited to T2D, cancer, and sleep disorders.

Methods

Design and expression of MT_2-CC

The DNA sequence of human MT_2 receptor (UniProt[20] identifier P49286) was synthesised by GenScript with optimisation for expression in insect cells. The crystallised construct (MT_2-CC) has truncations of N-terminal residues 1–30 and C-terminal residues 341–362. The thermostabilised apocytochrome b_{562}RIL (BRIL, UniProt P0ABE7) from *Escherichia coli* with mutations M7W, H102I, and R106L was fused to the truncated N-terminus of MT_2 with a six-residue linker (amino acid sequence GDGARP). Another fusion protein, rubredoxin (Rub, Uniprot P00268), was fused in the ICL3, replacing receptor residues 232–240. For construct optimisation (to increase monodispersity, thermostability, and crystallisability), the following point mutations were added: D86$^{2.50}$N[9], L108^{ECL1}F, F129$^{3.41}$W[10], N137$^{3.49}$D, C140$^{3.52}$L, W264$^{6.48}$F, A305$^{7.50}$P, and N312$^{8.47}$D (see the accompanying paper for details[8]). The MT_2-CC coding sequence was subcloned into a modified pFastBac1 (Invitrogen) vector, with a haemagglutinin (HA) signal sequence and a Flag tag on the N-terminus and a PreScission protease cleavage site followed by a 10×His tag on the C-terminus. The receptor was expressed in *Spodoptera frugiperda* cells (Sf9, purchased from ATCC, CRL-1711, authenticated by supplier using morphology and growth characteristics, certified mycoplasma-free), which were harvested and stored as described in the accompanying paper[8].

Purification of MT_2-CC

Insect cell membranes were prepared by thawing frozen cell pellets in a hypotonic buffer containing 10 mM HEPES (pH 7.5), 10 mM $MgCl_2$, 20 mM KCl, and homemade protease

inhibitor cocktail. Extensive washing of the raw membranes was performed by repeated Dounce homogenisation and centrifugation in hypotonic buffer (once), followed by high osmotic buffer containing 1.0 M NaCl, 10 mM HEPES (pH 7.5), 10 mM $MgCl_2$, 20 mM KCl, and homemade protease inhibitor cocktail (two or three times), thereby separating soluble and membrane associated proteins from integral membrane proteins. Stocks (100 mM) of 2-pmt (Tocris) and ramelteon (Apex Biosciences) were dissolved in DMSO. Washed membranes were resuspended into a buffer containing 50 μM 2-pmt or ramelteon, 2 mg ml^{-1} iodoacetamide, and homemade protease inhibitor cocktail, and incubated at 4 °C for 30 min before solubilisation. The membranes were then solubilised in 50 mM HEPES (pH 7.5), 150 mM NaCl, 1% (wt/vol) *n*-dodecyl-β-D-maltopyranoside (DDM, Anatrace), 0.2% (wt/vol) cholesteryl hemisuccinate (CHS, Sigma-Aldrich) at 4 °C for 3 h. The supernatant was isolated by centrifugation at 60,000×*g* for 50 min, and incubated in 20 mM HEPES (pH 7.5), 800 mM NaCl with Talon (immobilized metal affinity chromatography IMAC) resin (Clontech) overnight at 4 °C. After binding, the resin was washed with twenty column volumes of wash buffer 1 (50 mM HEPES (pH 7.5), 50 μM 2-pmt or ramelteon, 800 mM NaCl, 10% (vol/vol) glycerol, 0.1% (wt/vol) DDM, 0.02% (wt/vol) CHS, 10 mM imidazole), followed by ten column volumes of wash buffer 2 (50 mM HEPES (pH 7.5), 50 μM 2-pmt or ramelteon, 150 mM NaCl, 10% (vol/vol) glycerol, 0.05% (wt/vol) DDM, 0.01% (wt/vol) CHS, 50 mM imidazole). The protein was then eluted in minimal volumes of elution buffer (50 mM HEPES (pH 7.5), 50 μM 2-pmt or ramelteon, 150 mM NaCl, 10% (vol/vol) glycerol, 0.02% (wt/vol) DDM, 0.01% (wt/vol) CHS, 220 mM imidazole). PD MiniTrap G-25 columns (GE Healthcare) were used to remove imidazole. The protein was then treated overnight with His-tagged PreScission protease (Genscript) to cleave the C-terminal His-tag. PreScission protease and the cleaved C-terminal fragment were removed by binding to Talon IMAC resin for 1.5 h at 4 °C. The protein was collected as the TALON IMAC column flow-through. The ligand concentration was increased to 100 μM, and the protein was concentrated to 30–40 mg ml^{-1} with a 100 kDa molecular mass cut-off Vivaspin centrifuge concentrator (Sartorius).

Protein stability assays

The stability of purified MT_2-CC was analysed by the microscale thermostability assay[21] using Rotorgene (QIAGEN). Briefly, 1–5 μg of protein was mixed with 1.5 μM 7-diethylamino-3-(4′-maleimidylphenyl)-4-methylcoumarin (CPM) dye (2.5 mM stock in DMSO) in 25 mM HEPES pH 7.5, 150 mM NaCl, 0.02% DDM (wt/vol), 0.004% CHS (wt/vol), 10% glycerol (vol/vol), and indicated concentrations of compounds to a final volume of 100 μl. Samples were incubated for 15 min at 20 °C and then heated gradually from 25 °C to 95 °C at a rate of 2 °C min^{-1}, monitoring CPM fluorescence (excitation 365 nm, emission 460 nm). The melting temperature (T_m) was determined using the derivative of the resulting melting temperature curve after background subtraction using Prism 5 (GraphPad, San Diego, California, USA).

Crystallisation

Purified MT_2-CC in complex with 2-pmt or ramelteon was reconstituted into LCP by mixing it with molten lipid using a mechanical syringe mixer[13]. The protein–LCP mixture contained 40% (wt/wt) receptor solution, 54% (wt/wt) monoolein, and 6% (wt/wt) cholesterol.

Crystallisation trials were performed in 96-well glass sandwich plates (Marienfeld) using an NT8-LCP robot (Formulatrix) by dispensing 40 nl of protein-laden LCP and 800 nl of precipitant solution per well. Plates were incubated and imaged at 20 °C using an automatic incubator/imager (RockImager 1000, Formulatrix). Initial crystal hits were identified in a condition containing 100 mM HEPES, pH 6.8, 30% (vol/vol) PEG 400, 100 mM $NH_4CH_3CO_2$. These crystals, approximately 30×30×70 μm^3, were harvested using micromounts (MiTeGen) and flash frozen in liquid nitrogen for data collection at a microfocus synchrotron source. After extensive optimisation, the best crystals diffracted to about 3.0 Å resolution, but suffered from radiation damage, resulting in a 3.5 Å complete dataset. Additives had no effect on diffraction quality. Microcrystals for SFX data collection were prepared in gas-tight syringes (Hamilton) as previously described[22]. After optimisation, diffraction-quality crystals were obtained from 100 mM ADA pH 5.8–6.5, 24–28% (vol/vol) PEG 400, 10–200 mM $NH_4CH_3CO_2$, 50 μM 2-pmt or ramelteon, by injecting 5 μl of protein-laden LCP into 50 μl precipitant in syringes. Before loading the microcrystals into the LCP injector, excess precipitant was removed and 7.9 MAG lipid was added to the LCP to absorb any residual precipitant solution and to prevent crystalline phase formation upon rapid cooling when injecting LCP into vacuum[23].

Crystallographic data collection

Data collection was performed at the Coherent X-ray Imaging (CXI)[24] end station of the Linac Coherent Light Source (LCLS), which operated at a wavelength of 1.3 Å (9.83 keV) delivering individual X-ray pulses of 30 and 42 fs pulse duration and approximately 10^{11} photons per pulse focused into a spot size of approximately 1.5 μm in diameter using a pair of Kirkpatrick–Baez mirrors. Microcrystals (Extended Data Fig. 1b) of MT_2 (approximately 5×5×5 μm^3) were delivered in the LCP media using an LCP microextrusion injector[23] with 50 μm nozzle running at a flow rate of approximately 300 nl min^{-1}. Diffraction images were recorded at a rate of 7,200 patterns per minute (120 Hz) with the 2.3 Megapixel Cornell-SLAC Pixel Array Detector (CSPAD)[25]. Initial diffraction frames were corrected and filtered using the software package Cheetah[26]. A crystal “hit” was defined as an image containing a minimum of 20 diffraction peaks with a signal to noise ratio above 4 and a number of pixels above 3. After further refinement of parameters (peak detection, prediction, and integration), images were indexed using MOSFLM[27], DirAx[28], and XDS[29] and integrated and merged into a final dataset by CrystFEL v.0.6.3 software suite[30]. Integration radii of 3, 5, and 6 pixels with per pattern resolution cut-offs 1.0 nm^{-1} above the conservative resolution estimates for each crystal were applied (*push-res* option), otherwise default values were used. The total numbers of collected images/hits/indexed images are as follows: 2,154,963/84,928/31,677 (MT_2-CC-2-pmt), 476,863/59,071/28,130 (MT_2-CC-H208A-2-pmt), 293,060/22.267/20,704 (MT_2-CC-N86D-2-pmt), 727,004/60,005/28,834 (MT_2-CC-ramelteon). As resolution cutoff, the criterion[31] of CC^*>0.5 was employed for all datasets (see Extended Data Table 2 for data statistics). The space group was determined to be $P2_1$, with two molecules per asymmetric unit.

Structure determination

To solve the 2.8 Å resolution MT_2-CC-2-pmt structure, a search model was generated as follows: the MT_2 receptor sequence was sent to the HHpred server[32], and the output models

were reduced by removing all low resolution (< 3.0 Å) and NMR structures. The PDB files of the top ten hits were downloaded and prepared with Sculptor[33]. The models were structurally superimposed, and the side chains were pruned, yielding the conserved receptor core model. The model that produced a successful molecular replacement (MR) solution with Phaser[34] (TFZ score of 14.9 and LLG of 320) was based on the C-C chemokine receptor 2 structure (PDB ID: 5T1A)[35]. This solution containing two receptor molecules was fixed as a partial solution, and the search continued with rubredoxin (PDB ID: 1IRO), where one molecule was placed in the asymmetric unit. The resulting three-component solution was subjected to several rounds of refining with phenix.refine[36] and model building with phenix.autobuild[37] followed by manual refinement in Coot[38]. BRIL (PDB ID: 1M6T) was then used independently as a search model for remaining fusion partners in the asymmetric unit. The second BRIL was manually modelled into the electron density; however, no density could be found for the second rubredoxin molecule, which, therefore, was not modelled in the final structure. This rubredoxin fusion partner is most likely disordered and does not participate in crystal contacts, however, there is space for it in the crystal lattice (Extended Data Fig. 1d). A zinc ion was modelled in rubredoxin as previously described[39]. Refinement and model completion were performed by repetitive cycling between Refmac5[40] or autoBUSTER[41] 2.10.2 and manual rebuilding in Coot[38] using both $2mF_o-DF_c$ and mF_o-DF_c maps. Ligand restraints for refinement of 2-pmt and ramelteon coordinates were generated by Prodrg[42]. For the other three datasets, the MT_2-CC-2-pmt structure was used as a search model for MR, and the refinement procedure was repeated as described above. The Ramachandran plot obtained by MolProbity[43] shows that with exception of Y92 from the YPYP motif all residues are in the favoured/allowed regions: 95.4/4.4% of residues (MT_2-CC-2-pmt), 93/6.8% of residues (MT_2-CC-H208A), 94.8/5.0% of residues (MT_2-CC-N86D), 95.3/4.5% of residues (MT_2-CC-ramelteon). Data collection and refinement statistics are summarised for each structure in Extended Data Table 2. Figures containing electron density and molecular structures were generated using PyMol[44].

Channel profile calculations

The channel diameter profile along its length was calculated with CAVER analyst v.2.0[45] using default parameters. Further details can be found in the accompanying paper[8].

Molecular docking

MT_2 receptor ligands obtained from the ChEMBL database[15] were docked into the 2-pmt-bound crystal structures using an energy based docking in ICM-Pro v3.8–6[46] as described in the accompanying paper[8].

Molecular dynamics simulations

The experimental structure of MT_2 was prepared and subjected to molecular dynamics simulations as described in the accompanying paper[8]. The simulation periodic box had dimensions (x, y, z) of 75.5 Å, 75.5 Å, 105.4 Å, and contained lipids (129 POPC molecules), 10,281 water molecules, 26 sodium, and 36 chloride ions.

Radioligand binding assays

Equilibrium binding assays were performed and analysed as described in the MT_1 paper[8]. HEK293T cells (purchased from ATCC, CRL-11268, authenticated by supplier using morphology, growth characteristics and STR profiling, certified mycoplasma-free). For kinetic studies, to initiate dissociation of [^{3}H]-melatonin, 10 μL of cold excess melatonin (10 μM) was added per well at specific time points ranging from 2 minutes to 10 hours, and immediately at time = 0 min plates were harvested. Dissociation experiments were performed at 25 °C for MT_1 and 37 °C for MT_2 because of the slow kinetics in MT_2. For all assays, non-specific activity was defined by the addition of 5 μM 2-pmt. Ligand dissociation data were analysed using "Dissociation-One phase exponential decay" to yield estimates of k_{off} using GraphPad Prism 5.0.

MT_2 Gi/o-mediated cAMP inhibition assay

MT_2 Gi/o-mediated cAMP inhibition assays were performed in HEK293T cells as described in the accompanying paper[8].

Extended Data

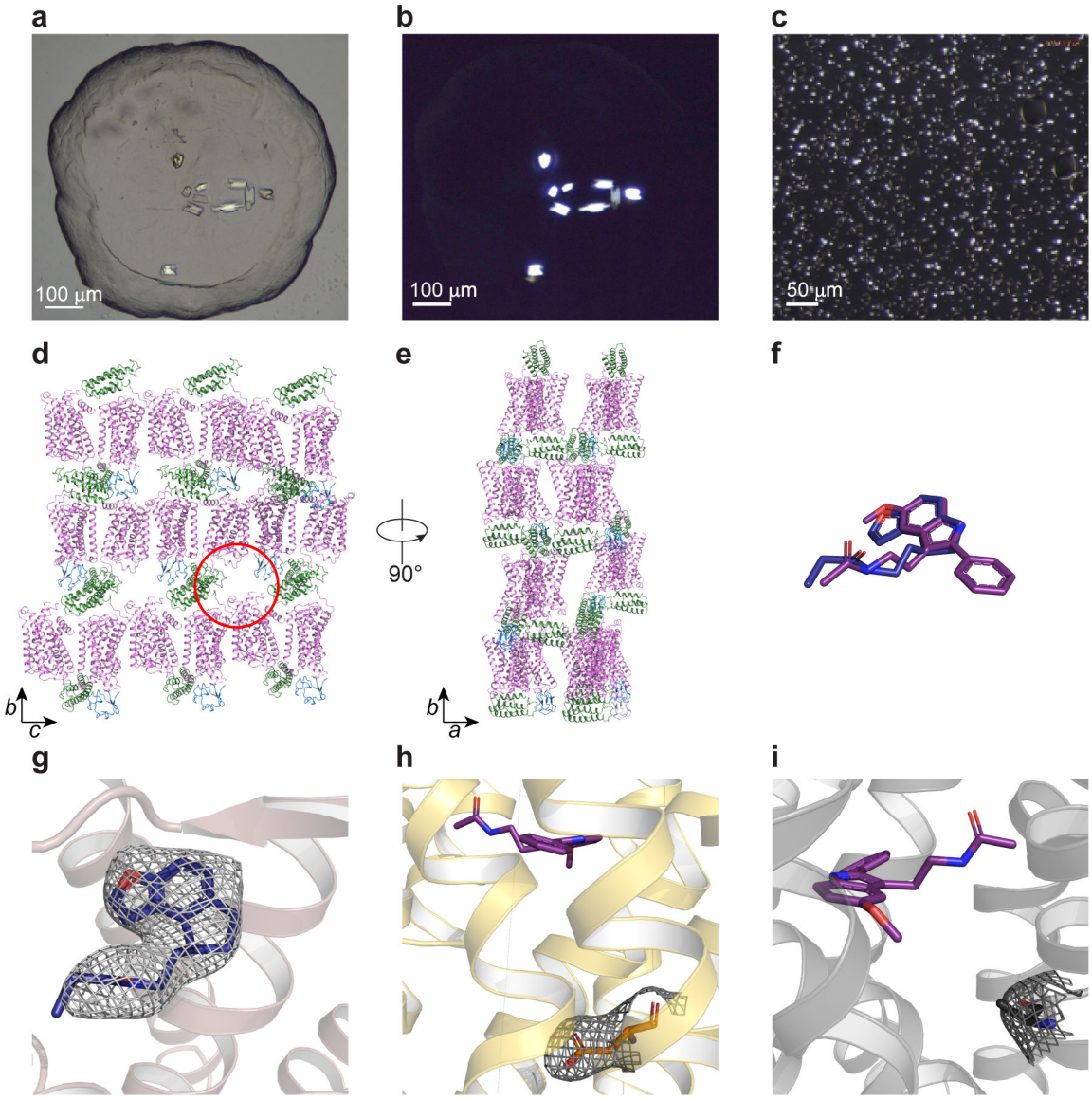

Extended Data Fig. 1 |. Crystallisation of MT_2: crystals, crystal packing, and electron density. **a,** Bright field and **b**, cross-polarised images of representative MT_2-2-pmt crystals optimized for synchrotron data collection (representing three independent crystallisation setups). **c,** cross-polarised image of representative MT_2-N86D-2-pmt crystals used for XFEL data collection (representing three independent crystallisation setups). See Extended Data Table 2 for data collection statistics. **d, e,** Crystal packing (receptor - purple, BRIL – green, and rubredoxin - blue). Space for missing rubredoxin in molecule B of the asymmetric unit is indicated with a red circle. Lattice rotated 90° is shown in **e**. **f,** Overlay of 2-pmt (purple) and ramelteon (blue) ligands of MT_2. **g-e**, $2mF_o$-DF_c density (grey) contoured at 1 σ of ramelteon (**g**), $N86^{2.50}D$ mutation (**h**), and $H208^{5.46}A$ mutation (**i**). 2-pmt is shown in purple.

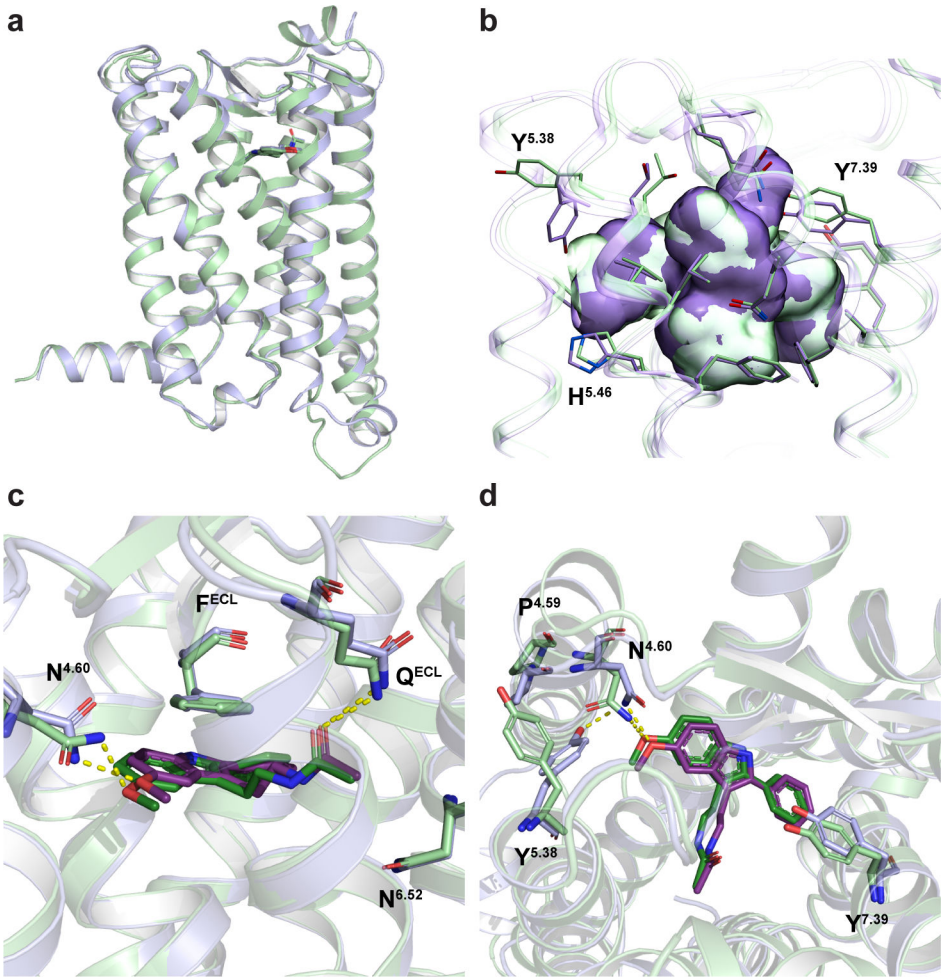

Extended Data Fig. 2 |. Structural differences between MT_1 and MT_2.

a, Overlay between MT_1-2-pmt (green) and MT_2-2-pmt (violet) structures (Cα r.m.s.d = 0.6 Å). **b**, Comparison of MT_1 (green) and MT_2 (violet) binding pockets. Overall, the binding pocket is about 50 $Å^3$ larger for MT_2. **c**, Comparison of 2-pmt ligand conformations in MT_1 (green) and MT_2 (violet). Hydrogen bonds are shown as yellow dashed lines. **d,** Overlay of MT_1 and MT_2, showing residues that display different conformations in the vicinity of the binding pocket. $N^{4.60}$ makes a hydrogen bond with $Y^{5.38}$ in MT_2 but not in MT_1.

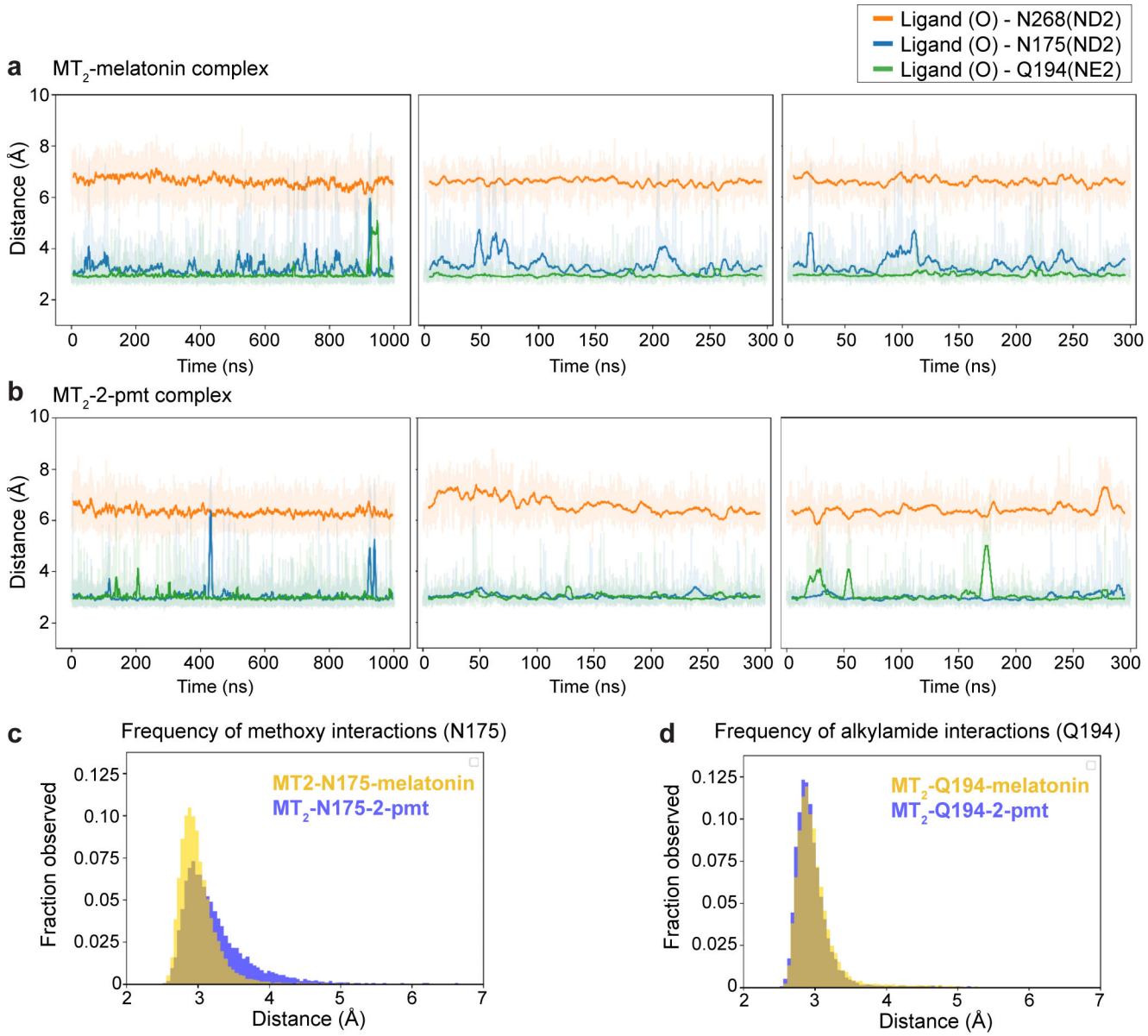

Extended Data Fig. 3 |. Molecular dynamics simulations.

a, b, Distance plots for interactions between residues in MT_2 ($N175^{4.60}$, atom type ND2 (N^{δ}); $Q194^{ECL2}$, atom NE2 (N^{ε}); $N268^{6.52}$, atom ND2), and closest oxygen atoms of the ligand methoxy and acetyl groups, respectively, in complexes with melatonin (**a**) and 2-pmt (**b**) from three independent simulations runs. **c,** Distance histograms for interactions of methoxy with $N175^{4.60}$ with melatonin (yellow) and 2-pmt (violet). **d**, Distance histograms for interactions of methoxy with and $Q194^{ECL2}$ with ligand alkylamide tail with melatonin (yellow) and 2-pmt (violet).

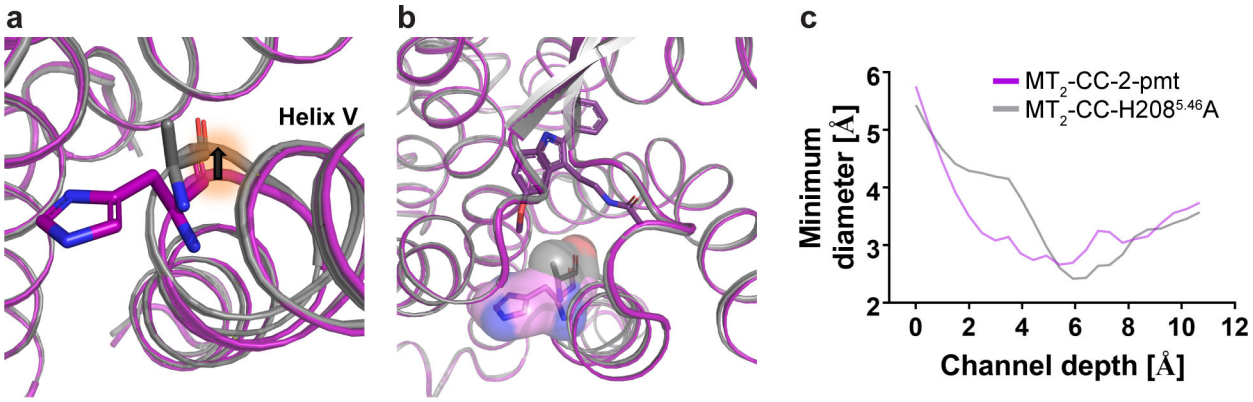

d

Mutant	melatonin			CTL 01-05-B-A05		
	EC_{50}, nM [n] (pEC_{50} ± s.e.m.)	$\%E_{MAX}$ ($\%E_{MAX}$*)	$\Delta\log(E_{MAX}/EC_{50})$ (mutant-wt)	EC_{50}, nM [n] (pEC_{50} ± s.e.m.)	$\%E_{MAX}$ ($\%E_{MAX}$*)	$\Delta\log(E_{MAX}/EC_{50})$ (mutant-wt)
WT	0.028 [16] (10.56±0.09)	100 (100)	0	16.59 [6] (7.78±0.07)	100 (63±7)	0
H208A (5.46)	0.190 [9] (9.72±0.26)	80±9	-0.93	*No agonist activity*		

Extended Data Fig. 4 |. Structural and functional differences between MT_2-pmt and MT_2-$H208A^{5.46}$-2-pmt.

a, Overlay of the MT_2-2-pmt (purple) structure with MT_2-$H208^{5.46}$A-2-pmt (grey) reveals an inward shift of helix V of ~0.9 Å due to the $H208^{5.46}$A mutation (as shown by black arrow). **b,** Surface representation of the $H208^{5.46}$ and $H208^{5.46}$A residues. Rotation of helix V renders the binding pocket volume ~50 $Å^3$ smaller for the $H208^{5.46}$A structure (binding site volume for MT_2-2-pmt: 766 $Å^3$ compared to 716 $Å^3$ for the MT_2-$H208^{5.46}$A structure). **c,** Comparison of the channel profiles (from the outside of the protein towards the ligand) for MT_2-2-pmt (purple) and MT_2-$H208^{5.46}$A-2-pmt (grey) reveals a narrowing of the MT_2-$H208^{5.46}$A-2-pmt channel around 6 Å as a consequence of the mutation and subsequent inward rotation of helix V. **d,** Functional data for WT and the $H208^{5.46}$A mutant expressed in HEK293T cells by using GloSensor to measure Gi/o-mediated cAMP inhibition. Data represent mean ± s.e.m. for n independent experiments as indicated in square brackets. $\%E_{MAX}$ is relative to wild-type receptor (in columns), and ($\%E_{MAX}$*) is relative to melatonin activity (in rows). See Methods for further information and Supplementary Figure 6 for dose response curves.

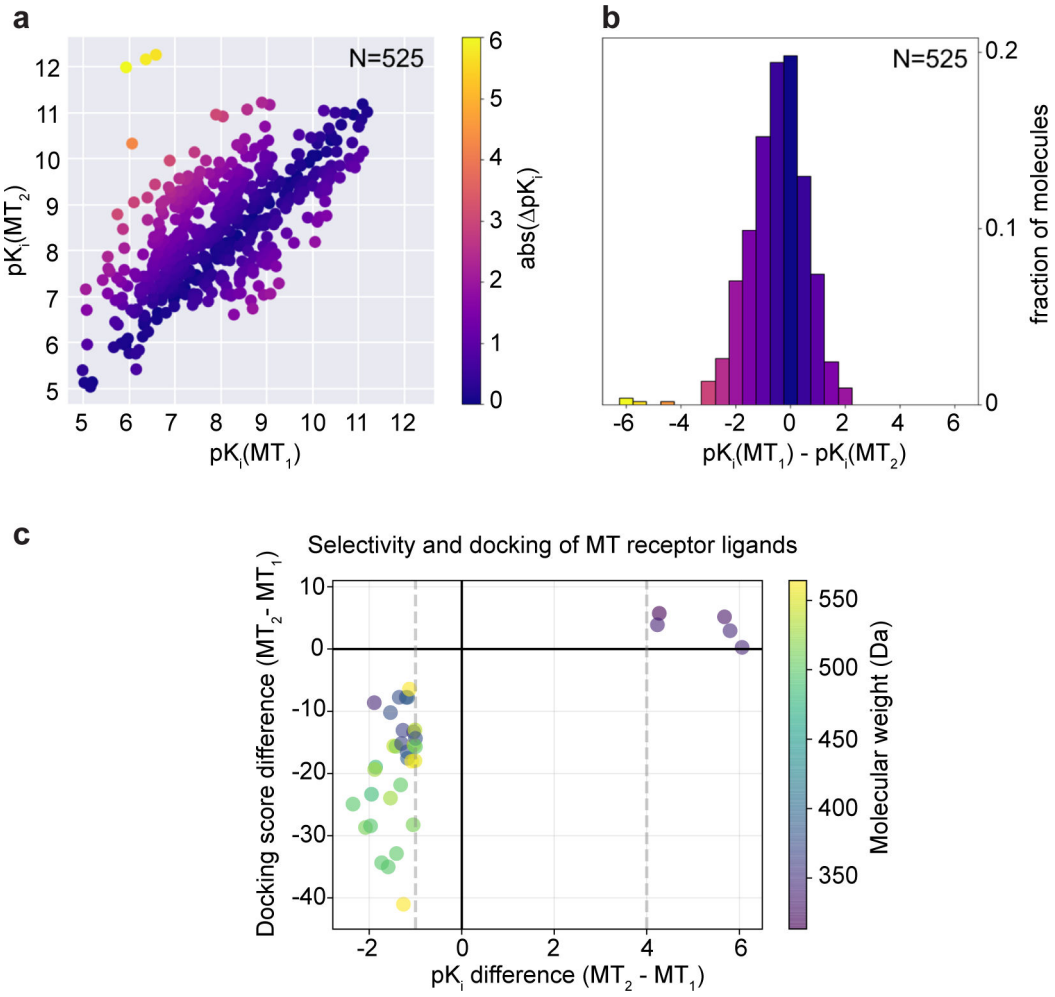

Extended Data Fig. 5 |. Selectivity analysis of melatonergic compounds.

a, Binding affinities of ligands for MT_1 (ChEMBL target identifier CHEMBL1945) and MT_2 (CHEMBL1946) were retrieved from the ChEMBL database[19] (v. 24) of experimental literature values. Of these ligands, 525 have affinities reported for both receptor subtypes. For ligands with multiple reported affinity values for a given receptor, pK_i values were averaged. MT_1-selective ligands are in the lower right quadrant; MT_2-selective ligands are in the upper left quadrant. Data points are coloured by absolute pK_i difference between subtypes, i.e. selectivity. **b,** Histogram of observed ligand selectivities. MT_2 selective ligands are on the left of the panel, MT_1 selective ligands are on the right. **c**, Plot of the docking score difference of select ligands that were docked between MT_2 and MT_1 versus their pK_i difference (MT_2-MT_1). Dashed lines indicate pK_i selectivity cutoff criteria (MT_1: 1 and MT_2: −4). Data points are colored by molecular weight (Da). See Supplementary Table 1 for details of docked ligands.

Extended Data Table 1 | Ligand affinity data for MT_2 mutants.

Data were acquired with MT_2 wild-type (WT) and mutants expressed in HEK293T cells by radioligand competition binding using [^{3}H]-melatonin (0.2–0.8 nM, unless otherwise indicated) to yield K_d or K_i affinity estimates. Data represent mean ± s.e.m. for n independent experiments as indicated in square brackets. Crystal constructs (CC) were expressed in Sf9 cells. ND, not determined. Binding isotherms are shown in Supplementary Figure 2. For determining the effect of NaCl, binding assays were performed in the presence of 147 nM NaCl (binding isotherms in Supplementary Figure 3).

Mutant	melatonin	2-pmt	ramelteon	agomelatine
	Kd, nM [n] (pK_d ±s.e.m.)	Ki, nM [n] (pK_i ±s.e.m.)	Ki, nM [n] (pK_i ±s.e.m.)	Ki, nM [n] (pK_i ±s.e.m.)
WT	0.54 [10] (9.27±0.12)	0.17 [10] (9.78±0.11)	0.23 [4] (9.66±0.10)	0.24 [4] (9.63±0.08)
WT + NaCl	1.56 [6] (8.81 ± 0.18)	ND	ND	ND
MT_2-CC (Sf9)	63.10 [3] (7.20±0.06)	3.14 [4] (8.50±0.06)	2.60 [4] (8.59±0.02)	6.88 [4] (8.16± 0.05)
MT_2-CC (sf9) + NaCl	48.23 [3] (7.32±0.03)	ND	ND	ND
MT_2-CC-N86$^{2.50}$D (Sf9)	29.40 [6] (7.53±0.34)	6.46 [4] (8.19±0.15)	7.37 [4] (8.13±0.09)	26.76 [4] (7.57±0.05)
MT_2-CC-H208$^{5.46}$A (Sf9)	10.81 [6] (7.97±0.16)	3.57 [6] (8.45±0.03)	2.03 [6] (8.69±0.13)	4.98 [6] (8.30±0.04)
D86N (2.50)	5.80 [3] (8.24±0.04)	0.33 [3] (9.48±0.12)	ND	ND
D86N (2.50) + NaCl	3.26 [3] (8.49±0.09)	ND	ND	ND
L108F (ECL1)	0.94 [3] (9.03±0.11)	0.13 [3] (9.87±0.15)	ND	ND
F129W (3.41)	2.84 [3] (8.55±0.04)	0.22 [3] (9.65±0.08)	ND	ND
N137D (3.49)	1.24 [3] (8.91±0.13)	0.12 [3] (9.92±0.00)	ND	ND
C140L (3.52)	0.21 [3] (9.68±0.05)	0.03 [3] (10.50±0.02)	ND	ND
W264F (6.48)	0.88 [3] (9.06±0.14)	0.06 [3] (10.25±0.26)	ND	ND
A305P (7.50)	3.94 [3] (8.40±0.19)	0.47 [3] (9.32±0.06)	ND	ND
N312D (7.57)	2.85 [3] (8.54±0.07)	0.36 [3] (9.44±0.04)	ND	ND
P95A (2.59)	*No specific binding up to 7 nM [^{3}H]-melatonin*			
M120A(3.32)	0.44 [3] (9.42±0.16)	0.028 [3] (10.7±0.3)	0.055 [3] (10.28±0.09)	0.052 [3] (10.35±0.18)
N175A(4.60)	0.86 [3] (9.2±0.3)	0.09 [3] (10.06±0.06)	0.08 [3] (10.12±0.11)	0.25 [3] (9.60±0.04)
F192A (ECL2)	*Low expression, no specific binding up to 7 nM [^{3}H]-melatonin*			
F192I (ECL2)	*No specific binding up to 7 nM [^{3}H]-melatonin*			

Mutant	melatonin	2-pmt	ramelteon	agomelatine
	Kd, nM [n] (pK_d ±s.e.m.)	Ki, nM [n] (pK_i ±s.e.m.)	Ki, nM [n] (pK_i ±s.e.m.)	Ki, nM [n] (pK_i ±s.e.m.)
Q194A (ECL2)	0.62 [3] (9.4±0.3)	0.043 [3] (10.38±0.07)	0.051 [3] (10.4±0.2)	0.12 [3] (9.94±0.09)
Y200A (5.38)	0.63 [3] (9.3±0.3)	0.14 [3] (9.86±0.01)	0.19 [3] (9.73±0.03)	0.67 [3] (9.18±0.02)
A203F(5.41)	0.82 [5] (9.09±0.01)	0.12 [5] (9.94±0.06)	0.19 [5] (9.47±0.19)	0.42 [5] (9.37±0.19)
H208A (5.46)	1.24 [3] (8.94±0.13)	0.17 [3] (9.79±0.09)	0.18 [3] (9.77±0.11)	0.22 [3] (9.68±0.11)
N268A (6.52)	0.96 [3] (9.3±0.4)	0.09 [3] (10.08±0.09)	0.12 [3] (9.92±0.05)	0.20 [3] (9.69±0.03)
Y294A (7.39)	1.07 [3] (8.99±0.09)	0.042 [3] (10.38±0.04)	0.049 [3] (10.33±0.09)	0.10 [3] (10.04±0.10)
Y308S (7.53)	*No specific binding up to 7 nM [^{3}H]-melatonin*			

Extended Data Table 2 | MT_2 Crystallographic data collection and refinement statistics.

	MT_2-CC-2-pmt[a]	MT_2-CC-H208$^{5.46}$A-2-pmt[b]	MT_2-CC-N86$^{2.50}$D-2-pmt[c]	MT_2-CC-ramelteon[d]
Data collection				
Space group	$P2_1$	$P2_1$	$P2_1$	$P2_1$
Cell dimensions				
a, b, c (Å)	69.5, 146.2, 77.3	69.2, 146.2, 77.3	68.7, 145.8, 77.0	69.4, 145.7, 77.2
α, β, γ (°)	90, 111.7, 90	90, 105.2, 90	90, 107.4, 90	90, 106.2, 90
Resolution (Å)	21.99–2.80 (2.88–2.80)	21.99–3.20 (3.34–3.20)	22.0–3.10 (3.23–3.10)	22.0–3.30 (3.46–3.30)
R_{split}	0.146 (4.31)	0.181 (3.26)	0.189 (4.70)	0.201 (2.90)
$I/\sigma I$	3.07 (0.46)	4.02 (0.39)	3.87 (0.2)	3.67 (0.42)
CC*	0.999 (0.52)	0.997 (0.54)	0.997 (0.60)	0.997 (0.54)
Completeness (%)	100 (100)	100 (100)	100 (100)	100 (100)
Redundancy	571.2 (141.3)	196.6 (39)	133 (38.2)	221.1 (84.6)
Refinement				
Resolution (Å)	21.99–2.80	21.99–3.20	22.0–3.10	22.0–3.30
No. reflections	35,193	24,439	26,179	22,122
R_{work}/R_{free}	0.219/0.249	0.224/0.250	0.234/0.262	0.248/0.270
No. atoms	A B	A B	A B	A B
Protein	3,333 2,852	3,343 2,786	3,293 2,752	3,227 2,738
Ligand/Zn^{+2}	23/1 23/0	23/1 23/0	23/1 23/0	19/1 19/0
Lipid and other	0 11	0 12	0 0	0 0
B-factors (Å^2)				
Receptor	116.4 121.0	95.0 99.6	114.2 117.2	114.1 118.2
BRIL	162.3 188.9	143.2 176.4	167.6 208.8	185.3 248.1
Rubredoxin	114.7 n/a	100.3 n/a	116.2 n/a	118.6 n/a
Ligand/Zn^{+2}	101.6/114.7 106.1/n/a	73.3/91.2 88.7/n/a	96.9/112.3 102.1/n/a	94.9/117.7 105.6/n/a

	MT_2-CC-2-pmt[a]		MT_2-CC-H208$^{5.46}$A-2-pmt[b]		MT_2-CC-N86$^{2.50}$D-2-pmt[c]		MT_2-CC-ramelteon[d]	
Lipids and other	n/a	138.8	n/a	111.0	n/a	n/a	n/a	n/a
R.m.s. deviations								
Bond lengths (Å)	0.009		0.010		0.009		0.009	
Bond angles (°)	0.97		1.06		0.96		0.95	

Footnote: Number of crystals used for structure determination:

[a] 31,677,

[b] 28,130,

[c] 20,704, and

[d] 28,834.

Values in parentheses are for highest-resolution shell.

Extended Data Table 3 | Functional data (Gi/o GloSensor) for MT_2crystal construct mutants.

Data were acquired with MT_2 wild-type (WT) and mutants expressed in HEK293T cells by using GloSensor to measure Gi/o-mediated cAMP inhibition via isoproterenol stimulation. Data represent mean ± s.e.m. for n independent experiments as indicated in square brackets. $\%E_{MAX}$ is relative to wild-type receptor (in columns), and ($\%E_{MAX}$*) is relative to melatonin (in rows). Mutant effects were calculated by the change in relative activity or log(Emax/EC50) subtracting WT from mutant. Dose-response curves are shown in Supplementary Figure 4.

Mutant	melatonin			2-pmt		
	EC_{50}, nM [n] (pEC_{50} ±s.e.m.)	$\%E_{MAX}$ ($\%E_{MAX}$*)	Δlog(E_{MAX} / EC_{50}) (mutant-WT)	EC_{50}, nM [n] (pEC_{50}±s.e.m.)	% E_{MAX} ($\%E_{MAX}$*)	Δlog(E_{MAX} / EC_{50}) (mutant-WT)
WT	0.028 [16] (10.56±0.09)	100 (100)	0	0.018 [14] (10.75±0.11)	100 (100±5)	0
MT_2-CC (Sf9)	*No activity*					
MT_2-Rub	*No activity*					
D86N (2.50)	3.951 [3] (8.40±0.34)	80±18 (100)	−2.25	1.995 [3] (8.70±0.11)	101±17 (126±21)	−2.04
L108F (ECL1)	0.029 [5] (10.54±0.10)	72±4 (100)	−0.16	0.011 [6] (10.95±0.19)	80±8 (110±11)	0.11
F129W (3.41)	0.011 [6] (10.95±0.17)	128±9 (100)	+0.50	0.007 [6] (11.16+0.20)	128±7 (99±6)	0.52
N137D (3.49)	0.019 [6] (10.72±0.12)	88±6 (100)	−0.11	0.016 [6] (10.81±0.10)	90±5 (103±5)	0.19
C140L (3.52)	0.072 [7] (10.15±0.16)	90±8 (100)	−0.46	0.035 [6] (10.45±0.16)	89±6 (101 ±4)	−0.34
W264F (6.48)	0.044 [7] (10.36±0.09)	117±6 (100)	−0.13	0.020 [5] (10.70±0.40)	118±8 (101±6)	−0.03
A305P (7.50)	0.141 [7] (9.85±0.16)	129±5 (100)	−0.60	0.073 [5] (10.14±0.26)	143±4 (91 ±6)	−0.45
N312D (7.57)	0.069 [5] (10.16±0.15)	135±6 (100)	−0.26	0.041 [3] (10.39±0.18)	138±10 (102±8)	−0.21

Extended Data Table 4 | Functional data (Gi/o GloSensor) for MT$_2$ mutants.

Data were acquired with MT$_2$ mutants by using GloSensor to measure Gi/o-mediated cAMP inhibition via isoproterenol stimulation. Data represent mean ± s.e.m. for n independent experiments as indicated in square brackets. %E_{MAX} is relative to wild-type receptor (in columns), and (%E_{MAX}*) is relative to melatonin (in rows). Mutant effects were calculated by the change in relative activity, or log(E_{MAX} /EC_{50}) subtracting wild-type from mutant. ND, not determined. Dose-response curves are shown in Supplementary Figure 5.

	melatonin			2-pmt			ramelteon			agomelatine		
Mutant	EC_{50}, nM [n] (pEC_{50}±s.e.m.)	% E_{MAX} (%E_{MAX}*)	Δlog(E_{MAX} / EC_{50}) (mutant-wt)	EC_{50}, nM [n] (pEC_{50}±s.e.m.)	% E_{MAX} (%E_{MAX}*)	Δlog(E_{MAX} / EC_{50}) (mutant-wt)	EC_{50}, nM [n] (pEC_{50}±s.e.m.)	% E_{MAX} (%E_{MAX}*)	Δlog(E_{MAX} / EC_{50}) (mutant-wt)	EC_{50}, nM [n] (pEC_{50}±s.e.m.)	% E_{MAX} (%MAX*)	Δlog(E_{MAX} / EC_{50}) (mutant-wt)
WT	0.028 [16] (10.56±0.09)	100 (100)	0	0.018 [12] (10.75±0.11)	100 (100±4)	0	0.016 [12] (10.81±0.14)	100 (108±3)	0	0.018 [10] (10.75±0.12)	100 (105±4)	0
P95A (2.59)	*No activity*											
A171M (4.56)	0.075 [9] 10.13±0.14	66±9 (100)	−0.61	0.032 [8] 10.49±0.11	62±9 (94±14)	−0.46	0.031 [7] 10.51±0.19	67±9 (90±12)	−0.47	0.025 [6] 10.60±0.16	75±10 (107±15)	−0.27
N175A (4.60)	0.070 [9] (10.16±0.15)	74±10 (100)	−0.53	0.0192 [8] (10.72±0.12)	67±14 91±19	−0.20	0.010 [7] (11.00±0.21)	72±12 (87±14)	+0.05	0.015(7] (10.82±0.13)	71 ±7 (91±10)	0.08
F192A (ECL2)	99.235 [6] (7.00±0.26)	122±7 (100)	−3.46	4.808 [10] 8.32±0.09	139±3 (114±6)	−2.28	4.799 [9] 8.32±0.04	150±4 (109±3)	−2.31	5.316 [9] 8.27±0.05	145±2 (111±2)	−2.31
F192I (ECL2)	3.00 [3] (8.52±0.30)	159±4 (100)	−1.83	0.211 [3] (9.68±0.07)	159±3 (100±1)	−0.87	0.571 [3] (9.24±0.16)	169±5 (94±3)	−1.34	2.754 [3] (8.56±0.05)	160±8 (94±5)	−1.98
Q194A (ECL2)	0.025 [3] (10.60±0.22)	131±4 (100)	+0.16	0.011 [3] (10.96±0.08)	130±3 (99±3)	+0.33	0.006 [3] (11.23±0.10)	130±6 (88±4)	+0.54	0.005 [3] (11.30±0.13)	110±15 (78±10)	+0.59
Y200A (5.38)	0.517 [3] (9.29±0.32)	161±10 (100)	−1.06	0.009 [3] (11.07±0.08)	158±16 (98±10)	+0.53	0.014 [3] (10.86±0.07)	164±21 (90±10)	0.26	0.314 [3] (9.50±0.31)	149±14 (87±8)	−1.07
H208A (5.46)	0.190 [9] (9.72±0.26)	80±9 (100)	−0.93	0.101 [10] (10.00±0.15)	75±9 (93±11)	−0.88	0.035 [8] (10.45±0.28)	79±11 (88±12)	−0.46	0.083 [8] (10.08±0.26)	76±2 (89±3)	−0.79
N268A (6.52) Q194A	0.046 [3] (10.33±0.27)	141±10 (100)	−0.08	0.013 [3] (10.87±0.10)	140±8 (99±6)	+0.28	0.009 [3] (11.05±0.10)	132±9 (83±6)	+0.36	0.007 [3] (11.16±0.10)	112±4 (75±3)	+0.46
(ECL2)/ N268A (6.52)	2.405 [9] 8.62±0.21	116±7 (100)	−1.88	0.033 [10] 10.49±0.18	112±6 (96±5)	−0.21	0.136 [9] 9.87±0.15	121±7 (93±5)	−0.86	0.759 [8] 9.12±0.14	116±4 (94±4)	−1.56
Y294A (7.39)	0.460 [4] (9.34±0.15)	148±6 (100)	−1.05	0.008 [4] (11.12+0.11)	153+7 (94+9)	+0.56	0.008 [3] (11.11+0.09)	153±11 (114+11)	+0.48	0.015 [3] (10.83±0.20)	118±11 (143±12)	−0.15
Y308S (7.53)	*No activity*											

Extended Data Table 5 | Thermostability data for MT$_2$ mutants.

Melting temperature T_m determined using the CPM assay[27] (mean ± s.d. for n=3 independent experiments) for the crystallised construct (MT$_2$-CC), and indicated mutants (in the MT$_2$-CC background), purified in absence (apo) and presence (100 μM) of ligand (mlt, melatonin and 2-pmt, 2-phenylmelatonin). ND, not determined. W129F refers to MT$_2$-CC but without the F129$^{3.41}$W mutation. Melting curves are shown in Supplementary Figure 7.

Mutant	apo Tm, °C	mlt Tm, °C	2-pmt Tm, °C	mlt ΔTm, °C	2-pmt ΔTm, °C
MT$_2$-CC	63.6±0.3	73.4±0.1	79.9±0.4	+9.8	+16.3
W129F (3.41)	59.0±0.2	72.4±0.1	78.9±0.3	+13.4	+19.9
N175A (4.60)	64.6±0.3	70.6±0.1	78.1±0.2	+6	+13.5
F192A (ECL2)	57.1±0.5	66.5±0.1	75.4±0.1	+9.4	+18.3
Q194A (ECL2)	65.5±0.3	69.9±0.3	77.3±0.2	+4.4	+11.8
H208A (5.46)	58.7±0.6	72.6±0.4	78.9±0.3	+13.9	+20.2
N268A (6.52)	63.3±0.3	66.1 ±0.2	74.6±0.3	+2.8	+11.3
Q194A (ECL2)/N268A (6.52)	67.9±0.3	67.9±0.1	71.4±0.3	0	+3.5
Y308S (7.53)	ND	65.5±0.2	75.8±0.3	ND	ND

Supplementary Material

Refer to Web version on PubMed Central for supplementary material.

Acknowledgements

We thank M. Chu, C. Hanson, K. Villers, and J. Velasquez for help with cloning and expression, T. Grant for XFEL data processing, and H. Shaye for technical support. This work was supported by the National Institutes of Health grants R35 GM127086 (V.C.), R21 DA042298 (W.L.), R01 GM124152 (W.L.), U24DK116195 (B.L.R.), R01MH112205 (B.L.R.), the NIMH Psychoactive Drug Screening Program and the Michael Hooker Distinguished Professorship to B.L.R., F31-NS093917 (R.H.J.O.), the STC Program of the National Science Foundation (NSF) through BioXFEL (No. 1231306) (U.W., W.L., N.A.Z., V.C.), NSF ABI grant 1565180 (C.L, N.Z., U.W.), HFSP long-term fellowship LT000046/2014-L (L.C.J.), postdoctoral fellowship from the Swedish Research Council (L.C.J.); EMBO ALTF 677–2014 (B.S.). Parts of this research were carried out at the LCLS, a National User Facility operated by Stanford University on behalf of the U.S. Department of Energy and is supported by the U.S. Department of Energy Office of Science, Office of Basic Energy Sciences under Contract No. DE-AC02–76SF00515. This research benefited from the use of credits from the National Institutes of Health (NIH) Cloud Credits Model Pilot, a component of the NIH Big Data to Knowledge (BD2K) program.

References

1. Ebisawa T, Karne S, Lerner MR & Reppert SM Expression cloning of a high-affinity melatonin receptor from Xenopus dermal melanophores. Proc Natl Acad Sci USA 91, 6133–6137 (1994). [PubMed: 7517042]
2. Reppert SM et al. Molecular characterization of a second melatonin receptor expressed in human retina and brain: the Mel1b melatonin receptor. Proc Natl Acad Sci USA 92, 8734–8738 (1995). [PubMed: 7568007]
3. Liu J et al. MT1 and MT2 Melatonin Receptors: A Therapeutic Perspective. Annu Rev Pharmacol Toxicol 56, 361–383 (2016). [PubMed: 26514204]
4. Bonnefond A et al. Rare MTNR1B variants impairing melatonin receptor 1B function contribute to type 2 diabetes. Nat Genet 44, 297–301 (2012). [PubMed: 22286214]
5. Karamitri A et al. Type 2 diabetes-associated variants of the MT2 melatonin receptor affect distinct modes of signaling. Sci Signal 11, eaan6622 (2018). [PubMed: 30154102]
6. Kato K et al. Neurochemical properties of ramelteon (TAK-375), a selective MT1/MT2 receptor agonist. Neuropharmacology 48, 301–310 (2005). [PubMed: 15695169]
7. Ballesteros JA, Weinstein H Integrated methods for the construction of three-dimensional models and computational probing of structure-function relations in G protein-coupled receptors. 25, 366–428 (1995).
8. Stauch B, et al. Structural basis for ligand recognition at the human MT1 melatonin receptor. Nature accompanying manuscript (2019).
9. White KL et al. Structural Connection between Activation Microswitch and Allosteric Sodium Site in GPCR Signaling. Structure 26, 259–269 (2018). [PubMed: 29395784]
10. Roth CB, Hanson MA & Stevens RC Stabilization of the human beta2-adrenergic receptor TM4-TM3-TM5 helix interface by mutagenesis of Glu122(3.41), a critical residue in GPCR structure. J Mol Biol 376, 1305–1319 (2008). [PubMed: 18222471]
11. Chun E et al. Fusion partner toolchest for the stabilization and crystallization of G protein-coupled receptors. Structure 20, 967–976 (2012). [PubMed: 22681902]
12. Audet M & Bouvier M Restructuring G-protein- coupled receptor activation. Cell 151, 14–23 (2012). [PubMed: 23021212]
13. Caffrey M & Cherezov V Crystallizing membrane proteins using lipidic mesophases. Nat Protoc 4, 706–731 (2009). [PubMed: 19390528]
14. Rivara S, Mor M, Bedini A, Spadoni G & Tarzia G Melatonin receptor agonists: SAR and applications to the treatment of sleep-wake disorders. Curr Top Med Chem 8, 954–968 (2008). [PubMed: 18673165]

15. Bento AP et al. The ChEMBL bioactivity database: an update. Nucleic Acids Res 42, D1083–1090 (2014). [PubMed: 24214965]
16. Nonno R et al. A new melatonin receptor ligand with mt1-agonist and MT2-antagonist properties. J Pineal Res 29, 234–240 (2000). [PubMed: 11068946]
17. Zlotos DP, Jockers R, Cecon E, Rivara S & Witt-Enderby PA MT1 and MT2 melatonin receptors: ligands, models, oligomers, and therapeutic potential. J Med Chem 57, 3161–3185 (2014). [PubMed: 24228714]
18. Teh MT & Sugden D Comparison of the structure-activity relationships of melatonin receptor agonists and antagonists: lengthening the N-acyl side-chain has differing effects on potency on Xenopus melanophores. Naunyn Schmiedebergs Arch Pharmacol 358, 522–528 (1998). [PubMed: 9840420]
19. Valentin-Hansen L et al. The arginine of the DRY motif in transmembrane segment III functions as a balancing micro-switch in the activation of the beta2-adrenergic receptor. J Biol Chem 287, 31973–31982 (2012). [PubMed: 22843684]
20. Consortium UniProt. UniProt: the universal protein knowledgebase. Nucleic Acids Res 46, 2699 (2018). [PubMed: 29425356]
21. Alexandrov AI, Mileni M, Chien EY, Hanson MA & Stevens RC Microscale fluorescent thermal stability assay for membrane proteins. Structure 16, 351–359 (2008). [PubMed: 18334210]
22. Liu W et al. Serial femtosecond crystallography of G protein-coupled receptors. Science 342, 1521–1524 (2013). [PubMed: 24357322]
23. Weierstall U et al. Lipidic cubic phase injector facilitates membrane protein serial femtosecond crystallography. Nat Commun 5, 3309 (2014). [PubMed: 24525480]
24. Boutet SW, The GJ Coherent X-ray Imaging (CXI) instrument at the Linac Coherent Light Source (LCLS). New Journal of Physics 12, 035024 (2010).
25. Hart P, Boutet S, Carini G, Dubrovin M, Duda B, Fritz D, et al. The CSPAD megapixel x-ray camera at LCLS. Moeller SP, Yabashi M, & Hau-Riege SP (Eds.), 8504, 85040C–85012 (2012).
26. Barty A et al. Cheetah: software for high-throughput reduction and analysis of serial femtosecond X-ray diffraction data. J Appl Crystallogr 47, 1118–1131 (2014). [PubMed: 24904246]
27. Battye TG, Kontogiannis L, Johnson O, Powell HR & Leslie AG iMOSFLM: a new graphical interface for diffraction-image processing with MOSFLM. Acta Crystallogr D Biol Crystallogr 67, 271–281 (2011). [PubMed: 21460445]
28. Duisenberg AJM Indexing in Single-Crystal Diffractometry with an Obstinate List of Reflections J. Appl. Cryst 25, 92–96 (1992).
29. Kabsch W Xds. Acta Crystallogr D Biol Crystallogr 66, 125–132 (2010). [PubMed: 20124692]
30. White TA et al. Recent developments in CrystFEL. J Appl Crystallogr 49, 680–689 (2016). [PubMed: 27047311]
31. Karplus PA & Diederichs K Linking crystallographic model and data quality. Science 336, 1030–1033 (2012). [PubMed: 22628654]
32. Zimmermann L et al. A Completely Reimplemented MPI Bioinformatics Toolkit with a New HHpred Server at its Core. J Mol Biol 430, 2237–2243 (2018). [PubMed: 29258817]
33. Bunkoczi G & Read RJ Improvement of molecular-replacement models with Sculptor. Acta Crystallogr D Biol Crystallogr 67, 303–312 (2011). [PubMed: 21460448]
34. McCoy AJ et al. Phaser crystallographic software. J Appl Crystallogr 40, 658–674 (2007). [PubMed: 19461840]
35. Zheng Y et al. Structure of CC chemokine receptor 2 with orthosteric and allosteric antagonists. Nature 540, 458–461 (2016). [PubMed: 27926736]
36. Afonine PV et al. Towards automated crystallographic structure refinement with phenix.refine. Acta Crystallogr D Biol Crystallogr 68, 352–367 (2012). [PubMed: 22505256]
37. Adams PD et al. PHENIX: a comprehensive Python-based system for macromolecular structure solution. Acta Crystallogr D Biol Crystallogr 66, 213–221 (2010). [PubMed: 20124702]
38. Emsley P, Lohkamp B, Scott WG & Cowtan K Features and development of Coot. Acta Crystallogr D Biol Crystallogr 66, 486–501 (2010). [PubMed: 20383002]

39. Tan Q et al. Structure of the CCR5 chemokine receptor-HIV entry inhibitor maraviroc complex. Science 341, 1387–1390 (2013). [PubMed: 24030490]

40. Murshudov GN, Vagin AA & Dodson EJ Refinement of macromolecular structures by the maximum-likelihood method. Acta Crystallogr D Biol Crystallogr 53, 240–255 (1997). [PubMed: 15299926]

41. BUSTER v. 2.10.2.

42. Schuttelkopf AW & van Aalten DM PRODRG: a tool for high-throughput crystallography of protein-ligand complexes. Acta Crystallogr D Biol Crystallogr 60, 1355–1363 (2004). [PubMed: 15272157]

43. Chen VB et al. MolProbity: all-atom structure validation for macromolecular crystallography. Acta Crystallogr D Biol Crystallogr 66, 12–21 (2010). [PubMed: 20057044]

44. The PyMOL Molecular Graphics System.

45. Jurcik A et al. CAVER Analyst 2.0: Analysis and Visualization of Channels and Tunnels in Protein Structures and Molecular Dynamics Trajectories. Bioinformatics (2018).

46. Abagyan RA, Totrov MM, Kuznetsov DA ICM: A New Method For Protein Modeling and Design: Applications To Docking and Structure Prediction From The Distorted Native Conformation. J. Comp. Chem 15, 488–506. (1994).

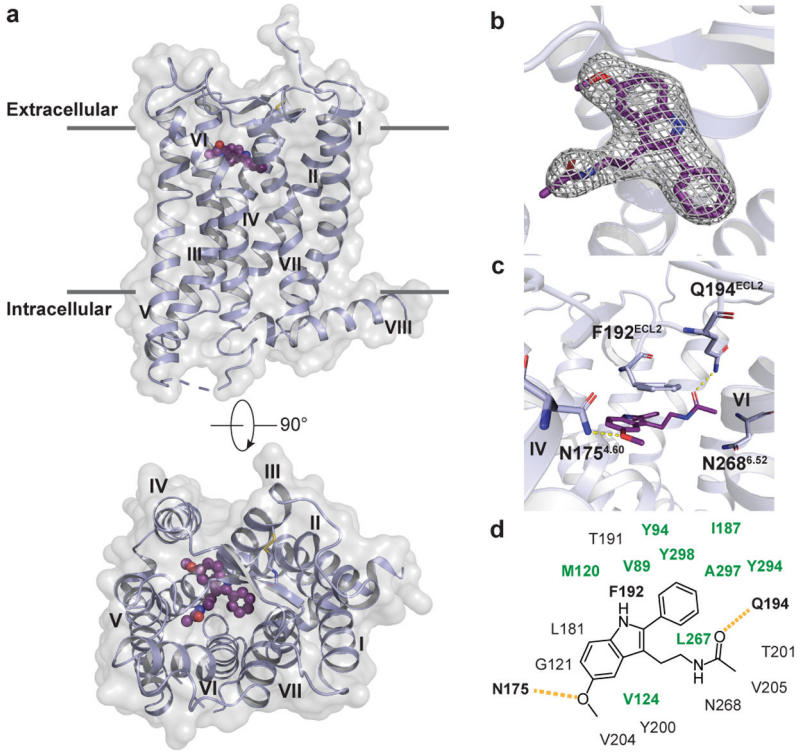

Fig. 1 |. Overview of the MT_2 structure.

a, Overview of MT_2 (violet) shows the canonical 7TM topology, with the ligand 2-pmt (purple) in the binding pocket. A 90° view shows the receptor from the extracellular side. Approximate membrane boundaries are shown as grey lines. **b,** $2mF_o$-DF_c density (grey mesh) of 2-pmt contoured at 1 σ. **c,** Binding pocket with key ligand interaction residues. **d,** Schematic diagram of ligand-interacting residues. Residues in the hydrophobic sub-pocket are coloured green. Hydrogen bonds are shown as dashed yellow lines in **c** and **d**.

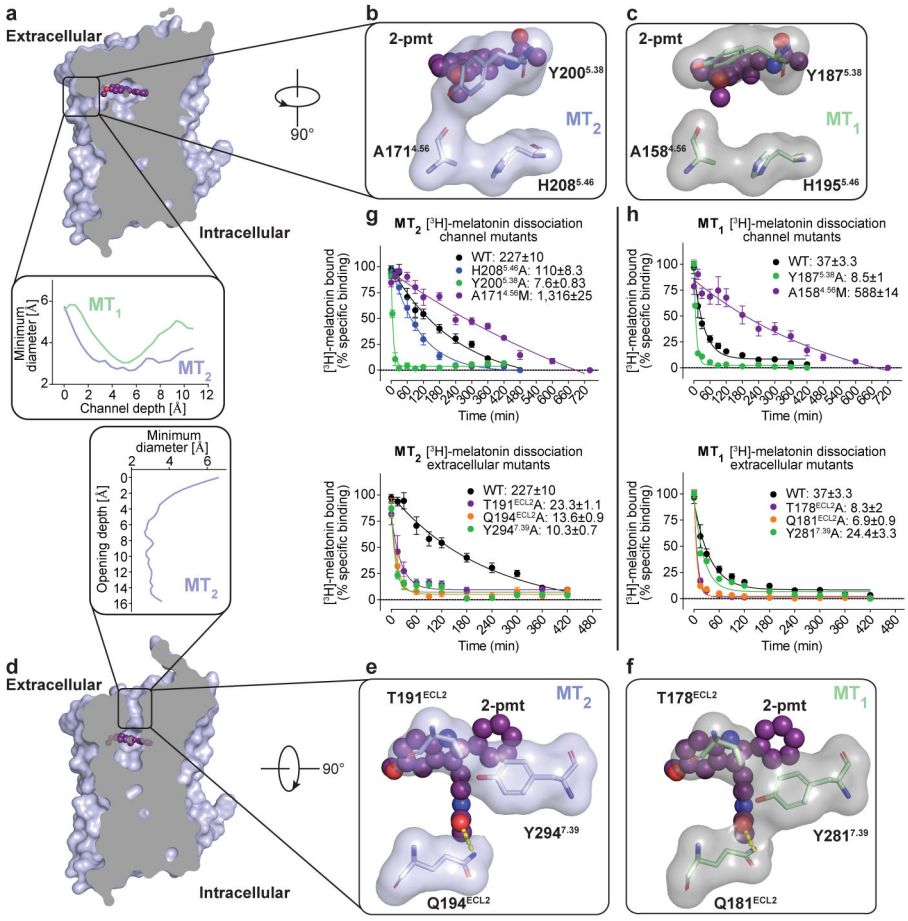

Fig. 2 |. Two possible ligand entries in MT_2.

a, View of the membrane-buried channel in MT_2. Insert shows the channel diameter profile across its length for MT_1 and MT_2. **b,** A 90° view of the channel in MT_2, highlighting three residues discussed in the text. **c,** The same as in **b** view of MT_1 (green) showing a different conformation of $Y187^{5.38}$ that widens the channel compared to MT_2. **d,** View of the ECL opening found in MT_2 (violet) with 2-pmt (purple). Insert shows the ECL opening profile across the length. **e,** A 90° view through the ECL opening in MT_2, highlighting three residues discussed in the text. **f**, The same as in **e** view of MT_1 (green), showing a different conformation of $Y281^{7.39}$ that seals the ECL opening. **g,** [^{3}H]-melatonin dissociation kinetics for MT_2 membrane channel mutants (top) and ECL opening mutants (bottom). **h,** same as in **g** for MT_1. Residence time ($1/k_{off}$) in **g** and **h** is given in minutes. Data are shown as mean±s.e.m. for n=3 independent experiments.

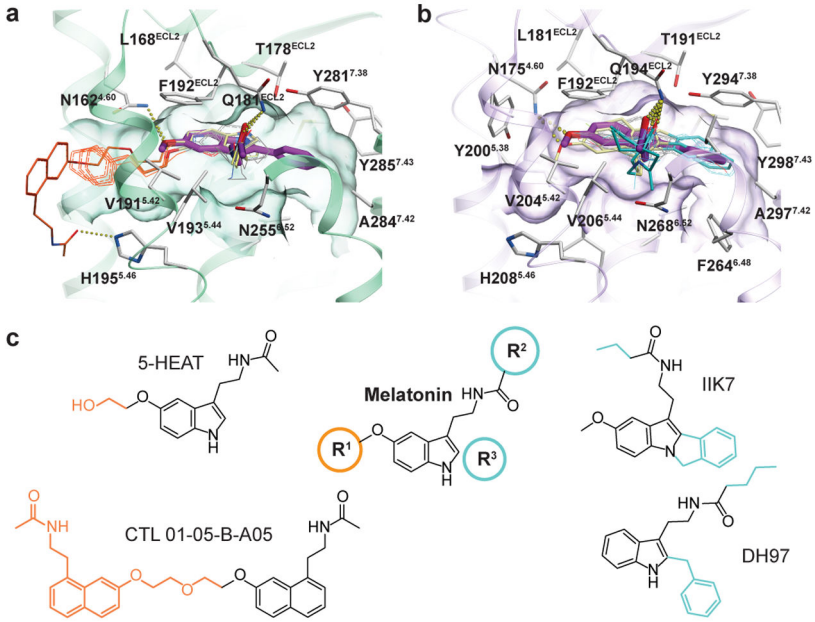

Fig. 3 |. Selectivity determinants of ligands at MT_1 and MT_2.

a, Docking of selective ligands into MT_1 (green), with 2-pmt (purple) from the crystal structure shown as reference. Ligands selective for MT_1 (compounds 63, 64, 65a, and 65b)[22] are shown in grey. Two representative ligands, 5-HEAT[16] and CTL 01–05-B-A05[8] are coloured pale yellow, with their selectivity-conferring substituents (R^1 position) shown in orange. **b,** Docking of ligands into MT_2 (violet), with 2-pmt (purple) shown as reference. Non-selective (tasimelteon, TIK301[22]) and selective (UCM1014, K185, and 4P-PDOT)[22] ligands are shown in grey. Two representative ligands, DH97[17] and IIK7[17] are coloured pale yellow, with selectivity-conferring substituents (R^2 and R^3 positions) shown in cyan. Predicted hydrogen bonds are shown as dotted lines in **a** and **b**. **c**, Melatonin SAR, where R^1 substituents confer MT_1 selectivity (orange), and substituents in R^2 and R^3 positions confer MT_2 selectivity (cyan). See Supplementary Table 1 for a list of all docked ligands.

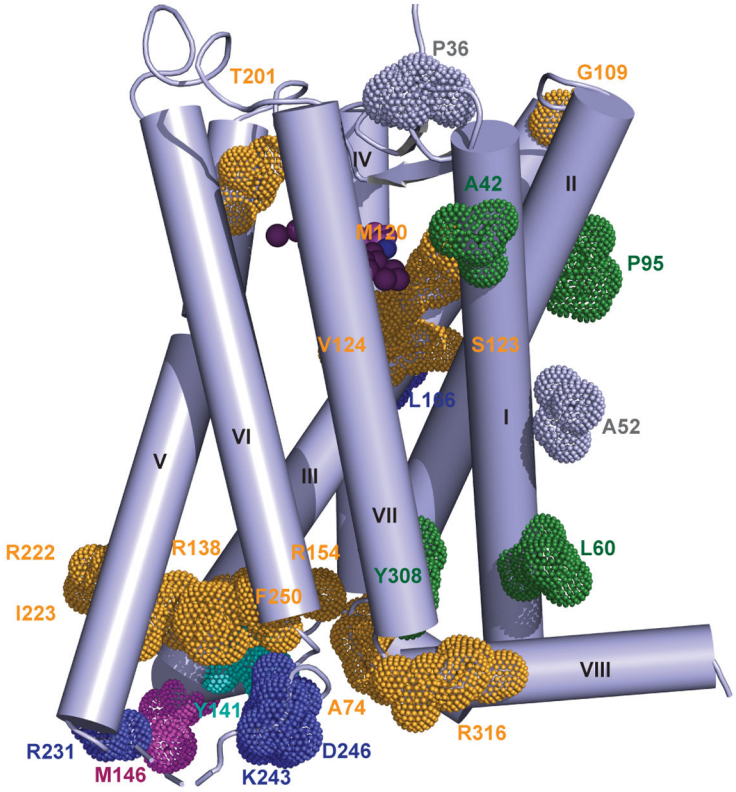

Fig. 4 |. MT_2 mutations implicated in type 2 diabetes.

Mapping of residues implicated in T2D as described in Refs.[4,5] on the MT_2 crystal structure. Residues, mutations of which lead to defects in two or more pathways, are coloured gold, G protein-specific defects - cyan, β-arrestin 2-specific - blue, ERK-specific – magenta, mutations abolishing melatonin-binding are shown in green, and those similar to WT shown in grey. T2D mutations in residues, not observed in the crystal structure, are not shown.